Nucleation and Aggregative Growth of Palladium Nanoparticles on Carbon Electrodes: Experiment and Kinetic Model

Yang-Rae Kim,[†] *Stanley C. S. Lai*,[†,‡] *Kim McKelvey*,[†] *Guohui Zhang*,[†] *David Perry*,[†§] *Thomas S. Miller,*[†] *Patrick R. Unwin**,[†]

[†]Department of Chemistry, University of Warwick, Coventry, CV4 7AL, United Kingdom

[‡]MESA+ Institute for Nanotechnology, University of Twente, PO Box 217, 7500 AE Enschede, The Netherlands

[§]MOAC Doctoral Training Centre, University of Warwick, Coventry, United Kingdom

ABSTRACT: The mechanism and kinetics of the electrochemical nucleation and growth of Pd nanoparticles (NPs) on carbon electrodes have been investigated using a microscale meniscus cell on both highly oriented pyrolytic graphite and a carbon coated transmission electron microscopy (TEM) grid. Using a microscale meniscus cell, it is possible to monitor the initial stage of electrodeposition electrochemically, while the ability to measure directly on a TEM grid allows subsequent high resolution microscopy characterization which provides detailed nanoscopic and kinetic information. TEM analysis clearly shows that Pd is electrodeposited in the form of NPs (approximately 1 − 2 nm diameter) that aggregate into extensive nanocrystal-type structures comprised of NPs. This gives rise to a high NP density. This mechanism is shown to be consistent with double potential step chronoamperometry measurements on HOPG, where a forward step generates electrodeposited Pd and the reverse step oxidizes the surface of the electrodeposited Pd to Pd oxide. The charge passed in these transients can be used to estimate the amounts of NPs electrodeposited and their size. Good agreement is found between the electrochemically determined parameters and the microscopy measurements. A model for electrodeposition based on the nucleation of NPs that aggregate to form stable structures is proposed that is used to analyze data and extract kinetics. This simple model reveals considerable information on the NP nucleation rate, the importance of aggregation in the deposition process and quantitative values for the aggregation rate.

KEYWORDS: electrochemistry, electrodeposition, electroplating, nanoclusters, nanofabrication, nanomaterials

INTRODUCTION

Metal nanoparticles (NPs) have attracted much interest because of their unique physicochemical properties, which differ from those of bulk materials.[1] In particular, NPs of a few nanometers in diameter exhibit size-dependent (electronic, optical, etc.) behavior[2], while in the area of (electro)catalysis, NP size and shape can have a profound impact on reaction rates and mechanisms.[3,4] Gaining control over the size of NPs is thus essential to enable their effective use in a variety of applications. Furthermore, the immobilization of NPs onto a solid substrate is often required for the fabrication of solid-state devices, yet the preparation and/or dispersion of NP (electro)catalysts of controlled size and distribution on a solid substrate remains a major challenge.[4] Several techniques have been used to fabricate substrate-supported NPs, such as lithographic methods (including e-beam lithography[5]), self-assembly[6], electrophoretic deposition[7] and electrodeposition[8].

Electrodeposition, the focus of this paper, is a promising approach that can be used to fabricate metal and metal oxide nanomaterials on conductive substrates, with several advantages over other methods.[4] In particular, electrodeposition is simple, convenient and cost-effective, as NPs grow directly from the substrate without the need for further sample preparation.[9] Moreover, neither photoresist nor surfactants are needed, ensuring that the nanomaterials remain in a close to pristine state. Electrodeposition also has the capability to enable the site-specific fabrication of nanostructures[10,11], and the composition and structure of materials can be tuned to some extent by changing the electrolyte composition and varying electrodeposition parameters, such as the concentration of metal ions in the precursor solution, the current density and the electrode potential. The latter two parameters offer the possibility of fabricating specific nanostructures through time-control.[12]

Although electrodeposition has several attributes, it can prove rather difficult to achieve a narrow size distribution of NPs using this methodology, at least in part due to insufficient understanding of the fundamental mechanisms of electrochemical nucleation and growth.[13] Investigations to improve knowledge in this area present a number of challenges. A major issue is that electrochemical nucleation sites of widely different character are randomly distributed on a solid substrate, and if there is a large number of nuclei and NPs, the interactions between them can be complex. There are many concepts involved in describing electrochemical nucleation and growth processes, including time-lag[14], nucleation exclusion zone[15] and the critical nuclei size[16], but their measurement and adaptation to the fabrication of NPs of controlled size is not straightforward. For improved electrodeposition at the nanoscale, full understanding of the mechanism of electrochemical nucleation and growth is essential, particularly for the initial stage of deposition.

Recently, several approaches for monitoring the early stages of nucleation have been reported. A liquid transmission electron microscopy (TEM) cell has been used to carry out both electrochemical measurements and *in situ* TEM imaging.[17,18] Discrepancies were found between apparent mechanistic inference from electrochemical data and TEM images. These experiments are rather difficult, particularly since obtaining reproducible liquid TEM cells is non-trivial and achieving clean electrode surfaces for employment in TEM cells can present some challenges due to the need for multiple lithography steps.[19] Some researchers have reported electron beam-assisted deposition of metal NPs using liquid-phase TEM systems.[20-22] Moreover, while *in situ* monitoring of the nucleation and growth of NPs was achieved, important information such as total charge transferred for the nucleation and growth of NPs was lost.[18] Furthermore, it was

found to be difficult to achieve delicate control of the driving force for these processes with the setups employed.

Pd electrodeposition on carbon electrodes allows the ready formation of effective electrocatalysts for formic acid-based fuel cells.[23] However, it is difficult to prepare small-sized Pd NPs using electrodeposition, which would be beneficial towards achieving higher catalytic mass activity.[24] In this paper, we report on the electrochemical production of Pd NPs using a microscale meniscus cell[25] on both highly oriented pyrolytic graphite (HOPG) and a carbon coated TEM grid, which serve as support electrodes. We have recently used this approach to study Ag electrodeposition on HOPG[26], revealing major new aspects to the process. Microscale meniscus landing[25] was performed using a solution-filled micropipet and the nucleation and growth processes were analyzed using cyclic voltammetry (CV) and chronoamperometry. This approach allows us to investigate the *entire substrate studied electrochemically* with *complementary microscopy techniques*. We demonstrate that the acquired TEM images are consistent with the aggregative growth mechanism recently suggested by Ustarroz and coworkers[13,27,28] and also seen in our Ag electrodeposition studies[26], in which the formation and aggregation of discrete NPs are the dominant processes. A simple new model is proposed to describe some of the features in the process that enables the analysis of experimental chronoamperometric data sets and provides mechanistic insight. These studies provide further considerable evidence for the importance of the aggregative growth mechanism in NP electrodeposition.

EXPERIMENTAL METHODS

Materials and characterization. All solutions were prepared using deionized water (Milli-Q, Millipore) with a resistivity of *ca*. 18.2 MΩ cm at 25ºC. All chemicals were used as received. Potassium tetrachloropalladate(II) (99.99%, Aldrich, UK) and perchloric acid (Acros) were used as the palladium precursor and electrolyte, respectively. HOPG (ZYB grade) was purchased from Aztech Trading, UK. This grade of HOPG gives rise to a relatively high step density on the basal surface compared to some other HOPG grades.[29]

HOPG was further considered as the main substrate in this work because it has been used extensively for electrochemical nucleation and growth studies[30-32] and is easily refreshed through cleavage.[29] For nanoscale imaging, a carbon film-coated 400 mesh gold (S160A4, Agar Scientific) TEM grid was used. This surface comprises amorphous carbon. TEM images were obtained using a JEOL 2000FX transmission electron microscope.

Experimental procedures. Borosilicate capillaries (1.2 mm outer diameter, 0.69 mm internal diameter, Harvard Apparatus Ltd.) were pulled using a laser pipet puller (P-2000, Sutter Instrument Co.) to produce micropipets with internal diameters of 2 or 5 μm. A 50 μm diameter micropipet was obtained by polishing a 5 μm diameter micropipet with a 0.1 μm grit polishing pad (Buehler). The pulled micropipets were coated on the outer wall with dichlorodimethylsilane (>99%, Acros) to produce a hydrophobic finish. Micropipets were filled with the aqueous electrolyte solution of interest and a home-made quasi-reference/counter electrode (QRCE), comprising a AgCl-coated Ag wire[33,34], was inserted. The freshly cleaved HOPG or the TEM

grid was used as a support electrode. The TEM grid was electrically connected to a copper wire *via* conductive silver epoxy.

The 50 μm diameter micropipet was mounted on a three-axis manual micromanipulator (Newport Corp.). The micropipet was lowered towards the substrate using the *z*-micromanipulator until the meniscus landed on the substrate.[8,25,35] A snapshot of a 50 μm diameter micropipet making meniscus contact with an HOPG substrate is shown in Figure 1(a).

The 2 μm diameter micropipet and substrate electrode were mounted on a *z*-piezoelectric positioner (P-753 LISA, Physik Intrumente) and *xy*-piezoelectric stage (P-621.2CL, Physik Instrumente), respectively. For measurements on the TEM grid, this setup was mounted on an inverted microscope (Axiovert 40, Zeiss) to facilitate positioning of the tip relative to the sample. The Ag/AgCl QRCE and the substrate were electrically connected to a custom homebuilt potentiostat and a current follower, respectively. Figure 1(b) shows a snapshot image of a 2 μm diameter micropipet close to the HOPG substrate prior to landing. The potentiostat and piezoelectric positioners were controlled through Labview code and an FPGA card (7852R, National Instruments).[29,33,36] A potential where no Pd electrodeposition occurred (1.0 V *versus* Ag/AgCl QRCE) was pre-applied to the substrate, but with the electrochemical cell at open-circuit as a consequence of the micropipet not being in meniscus contact with the substrate. The micropipet was slowly lowered and when the meniscus at the end of the micropipet touched the substrate, a current spike in the substrate current was generated, due to the connection of the electrochemical cell. This was used to halt the z-axis approach automatically. The CV and chronoamperometry experiments were subsequently performed (typically starting *ca*. 1 s after meniscus landing). The experimental scheme used for the microscale meniscus cell experiments is illustrated in Figure 1(c). For the chronoamperometry experiments, data acquisition was

typically performed at a rate of 165 μs per data point (each point from the average of 33 points acquired every 5 μs). Fitting of electrochemical data was carried out using ORIGIN 8.5 (Microcal Software Inc.).

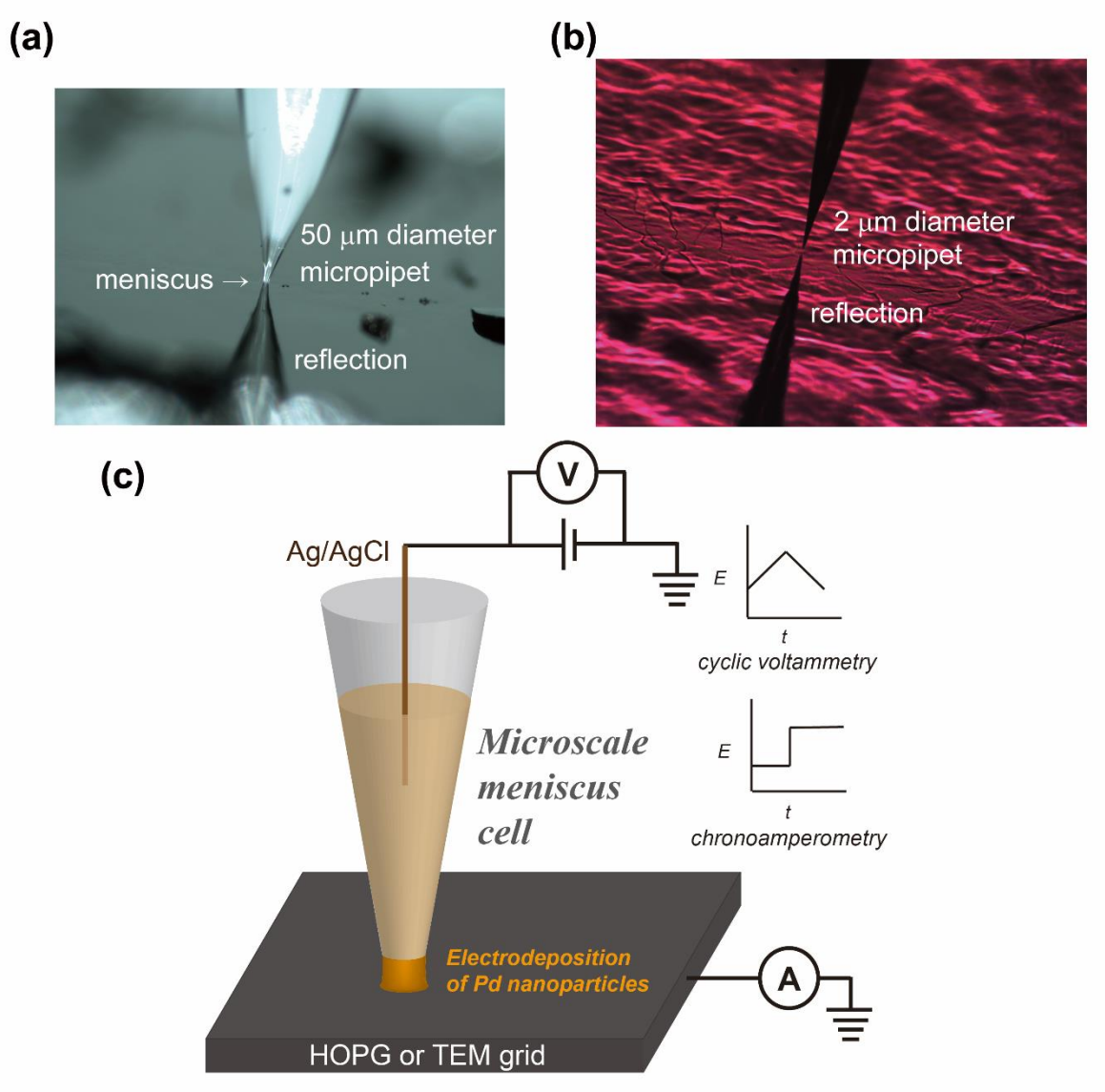

Figure 1. (a) Optical image of a 50 μm diameter micropipet in meniscus contact with an HOPG substrate. (b) A snapshot of a 2 μm diameter micropipet near HOPG prior to landing. (c)

Schematic of the microscale meniscus cell set up, as used for the studies of electrochemical nucleation and growth of Pd NPs with either a 2 or 50 μm diameter micropipet.

RESULTS AND DISCUSSION

To investigate the general characteristics of Pd electrodeposition on HOPG, CV data (20 mV s^{-1}) were obtained, over the potential range 1.0 V to -0.6 V in a solution of 1 mM K_2PdCl_4 and 0.1 M $HClO_4$ using a 50 μm diameter micropipet (Figure 2). In the first cycle, Pd electrodeposition started at an onset potential of 0.08 V, deduced from the sharp reduction peak. Further voltammetric features were observed in the potential range of -0.6 V to -0.2 V, which were due to oxygen reduction at Pd, *ca* -0.3 V, and hydrogen adsorption/desorption onto the surface and absorption into the palladium lattice, as evidenced by the sharp coupled peaks at -0.47 V and -0.3 V.[37] Another two broad oxidation peaks corresponding to the oxidation of Pd were found at around 0.37 V and 0.55 V on the reverse scan, respectively, similar to previous studies, with the more anodic peak assigned to pre-monolayer oxidation of palladium metal adatoms at the electrode.[37,38] In the second cycle, the reduction peak of Pd electrodeposition was broadened (also due to concomitant oxide reduction), and the onset potential was shifted significantly positive to 0.37 V, as expected for the growth of Pd on preformed Pd rather than on the carbon substrate.[37,39] In addition, the current magnitudes of two oxidation peaks were increased – particularly the more cathodic peak, corresponding to the formation of Pd oxide – and shifted slightly negative to 0.36 V and 0.51 V, respectively. These voltammetric features provide evidence for the nucleation and growth of Pd at the HOPG surface, with the magnitude and nature of the features strongly dependent on the voltammetric conditions, timescale and concentration of the Pd precursor in solution.[37,39] This electrochemical behavior is consistent with previous reports of Pd electrodeposition at the macroscale,[31,37] highlighting that the

microscale measurements do not introduce any new features or perturb this system compared to macroscopic studies.

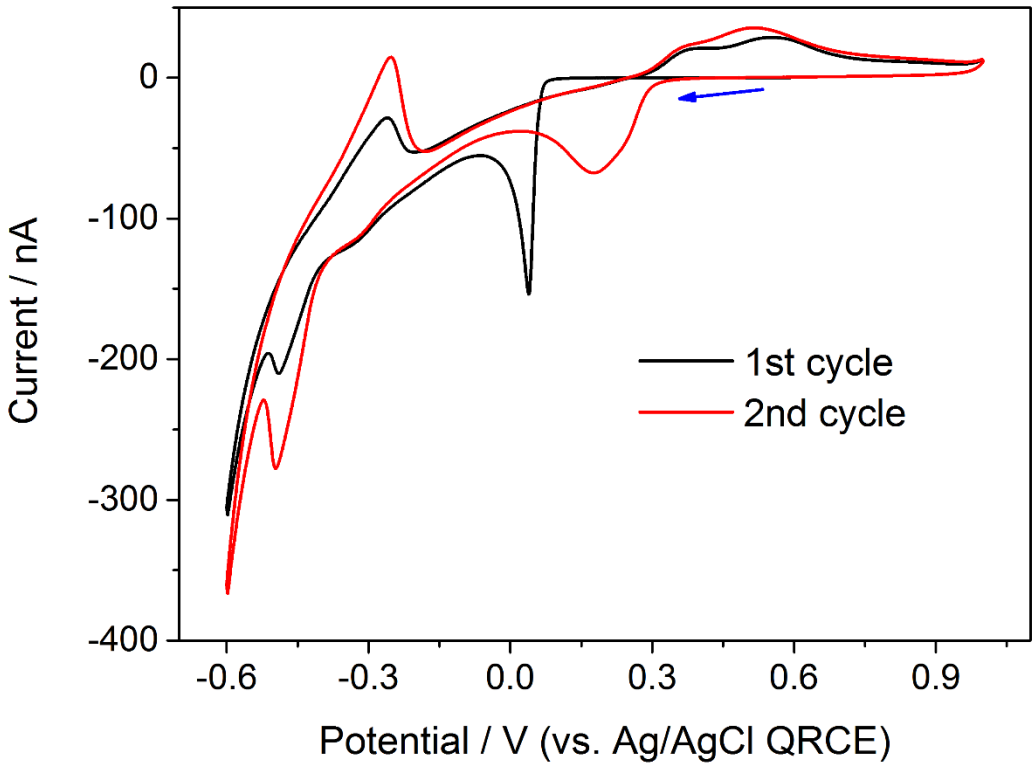

Figure 2. CV data for 1 mM K_2PdCl_4 in 0.1 M $HClO_4$ on HOPG at a scan rate of 20 mV s^{-1} using a 50 μm diameter micropipet. The arrow indicates the scan direction.

Having established the basic processes occurring during the electrodeposition of Pd on the 50 μm scale, we next used a 2 μm diameter micropipet to diminish the electroactive area by a factor of >500. On this scale, as we show herein, we are able to analyze in detail, by microscopy, electrodeposited material in the entire area studied for comparison to, and analysis of, the electrochemical data. Figure 3 shows CV data over 5 cycles for 1 mM K_2PdCl_4 and 0.1 M $HClO_4$ on HOPG at a scan rate of 0.2 V s^{-1}. The potential range was selected to focus on Pd electrodeposition and oxide formation, rather than other processes. In the first cycle, the reduction can be seen to start at a potential of 0.0 V, with the reduction peak becoming clearer and shifted to more positive values as the number of CV cycles increase. After five cycles, a clear reduction peak around 0.2 V is evident, indicating that the growth of Pd NPs was more favorable than the initial nucleation, consistent with the data on a larger scale (see above). In contrast to Figure 2, for potentials beyond 0 V, the current reaches a quasi-steady-state, consistent with non-linear diffusion (mass-transport) in pipets of this size, on this voltammetric time scale.[25] The current magnitude for the oxidation of Pd to Pd oxide in the potential range of 0.3 to 1.0 V is enhanced with increasing active electrochemical surface area caused by Pd electrodeposition during each cycle.

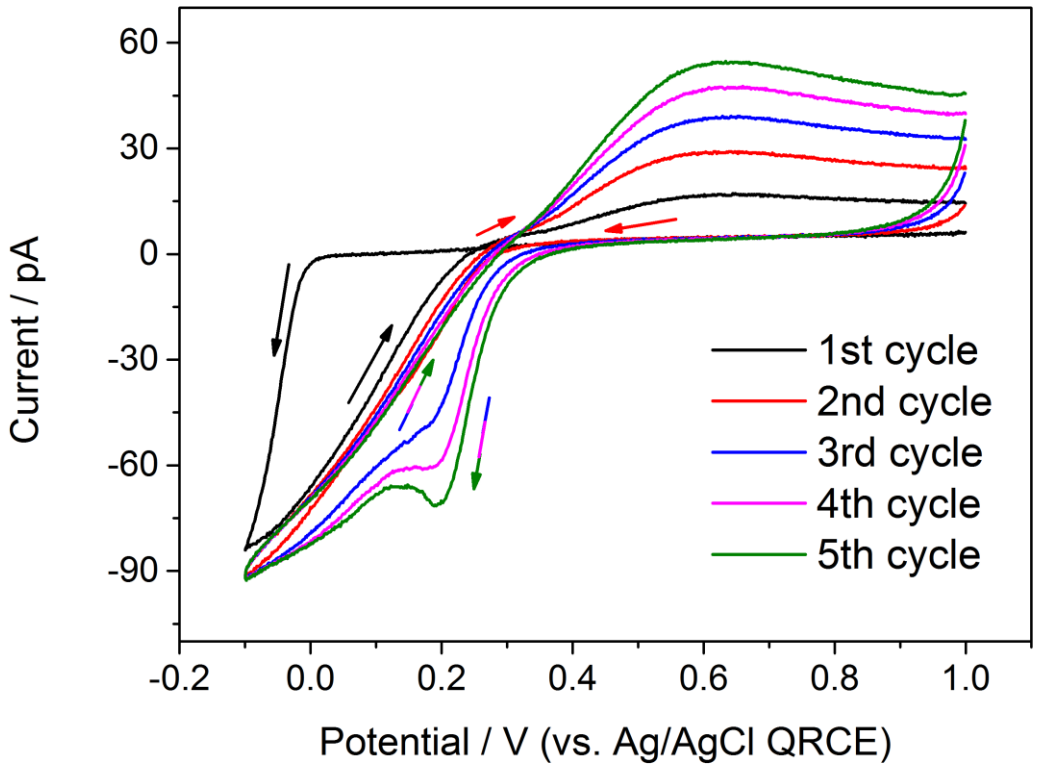

Figure 3. CV data (5 cycles) for 1 mM K_2PdCl_4 in 0.1 M $HClO_4$ on HOPG, with meniscus contact *via* a 2 μm diameter micropipet, at a scan rate of 0.2 V s^{-1}. The arrows indicate the scan direction, with the outward going (forward) scan starting at 1.0 V and progressing cathodically.

Potential step chronoamperometry is the preferred technique for monitoring electrochemical nucleation and growth processes, as this provides a constant (but controllable) driving force for electrodeposition, with the current-time behavior considered to inform on the rate and mechanism.[8,13,18,27,28] Here we used double potential step chronoamperometry (DPSC), jumping the potential from a value (1.00 V) where no reaction occurred, to different driving potentials for 1 s and then back to 1.00 V for 1 s, where the oxidation of Pd formed in the forward step (to Pd oxide) occurred, which could be used as an estimate of the surface area of the Pd electrodeposited, assuming negligible Pd electrodissolution (Figure 4); *vide infra*. Each measurement was made in a fresh spot on the HOPG substrate. There was no cathodic current at a driving of potential 0.20 V, indicating that no detectable Pd reduction occurred at this potential on this time scale. However, the reduction current at 0.05 V increased slowly after a period of about 0.3 s following the application of the electrode potential. Moreover, the total charge of the anodic current (8.59 pC), after stepping the potential back to 1.00 V was much higher than the anodic charge after reduction at 0.2 V (1.39 pC), consistent with the electrodeposition of Pd during the step to 0.05 V. Potential step chronoamperometry control measurements were also made by jumping the potential from 1.00 V to 0.05 V without the Pd precursor in the electrolyte (Figure S1, Supporting Information). Negligible current flow was detected. This confirms that the cathodic current with $PdCl_4^{2-}$ precursor was due to Pd reduction, and that Pd nucleation was initiated at potentials *ca.* 0.05 V and more cathodic on HOPG on this microscale.

As the overpotential increased, the shape of current–time curve changed. For a given time, the current magnitude was higher with increased driving potential. At a potential of 0.025 V, a plateau current was rapidly reached after approximately 0.5 s. It is evident that the *i-t* characteristic changed dramatically over a relatively small range of potential values (0.05 V to

0.025 V). That increasing amounts of Pd were electrodeposited with increasing driving potential is clear from the associated increased current flow in the reverse step (oxidation of Pd to Pd oxide).

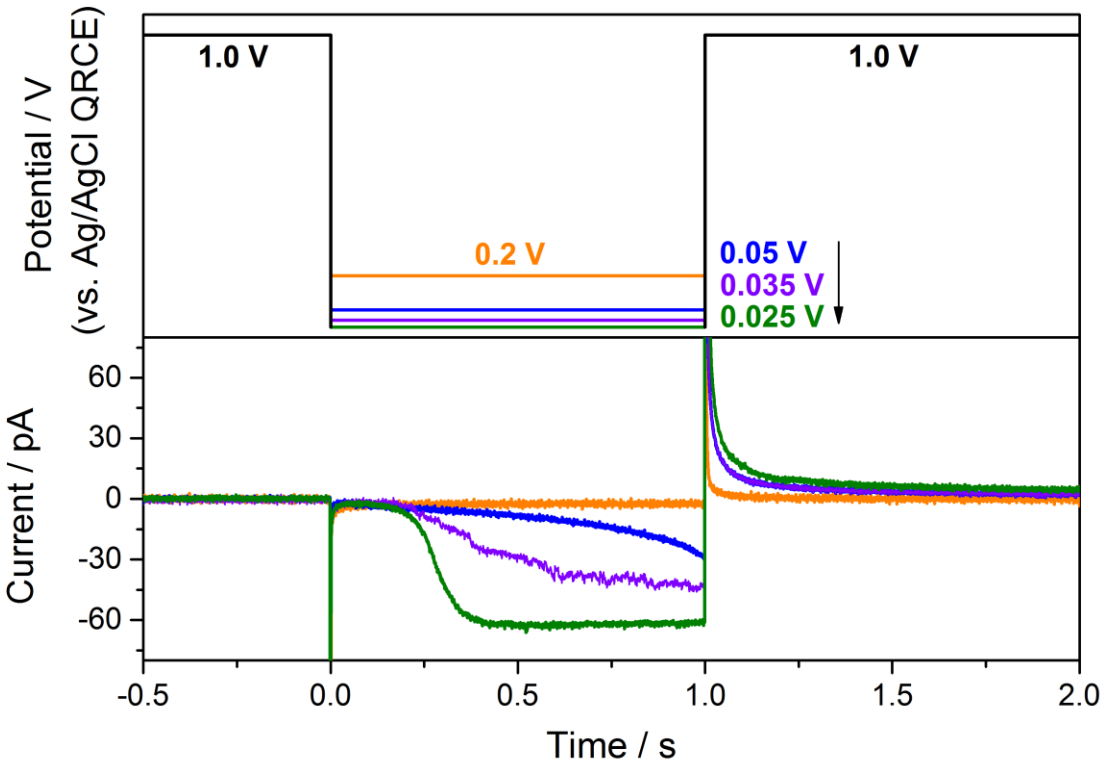

Figure 4. Chronoamperometry data for Pd electrodeposition on HOPG *via* meniscus contact with a 2 μm diameter micropipet at various driving potentials (forward potential step limit) in the range 0.2 V to 0.025 V for a period of 1 s, followed by a step to 1.0 V to promote Pd surface electro-oxidation for a further 1 s. The electrolyte was 1 mM K_2PdCl_4 in 0.1 M $HClO_4$.

To facilitate detailed kinetic and mechanistic analysis of nucleation and growth processes, comparison of electrochemical data with images of electrodeposited material is hugely valuable, with TEM being particularly powerful.[13,17] A carbon film-coated gold TEM grid was thus used as an electrode substrate for electrochemical measurements (see 'Experimental methods') and subsequent high resolution imaging of electrodeposited Pd. Figure S2 in Supporting Information shows typical CV data obtained for Pd electrodeposition on a TEM grid, and a chronoamperometric trace performed at a low driving potential of 0.05 V for 14 s is shown in Figure 5(a).

Although the potential of a clear reduction peak (0.20 V) on the TEM grid is similar to that (0.19 V) on the HOPG surface, in Figures 3 and S2, the kinetics appear slower on the TEM grid considering both the time-lag and the current magnitude. The time-lag before current flow during chronoamperometry on the TEM grid was estimated to be almost 2 s, which was longer than the 0.3 s recorded for HOPG (Figure 4), and the currents (for comparable times) are much smaller on the TEM grid than the HOPG surface. Furthermore, in comparison with HOPG, the current magnitude found in the CV and chronoamperometry experiments were smaller on the TEM grid (for similar times), with the appearance of a clear reduction peak in the CV requiring more 10 cycles on the TEM grid (compare Figure S2 in Supporting Information with Figure 3). While differences in wettability of these two carbon materials by meniscus contact might be a contributory factor, this effect is likely to be minimal as both substrates wet to the same extent (Figures 1b and S3a). Rather, our recent work has shown that while the nucleation of metals occurs readily at the basal surface of HOPG, step edges can act to trap electrodeposited nuclei,[26] and other work has indicated that steps are important in promoting the electrodeposition of NPs.[30] Such features are abundant on the ZYB grade HOPG used, but absent from the TEM grid,

which may explain the slower kinetics that are evident when the TEM grid is used as the electrode.

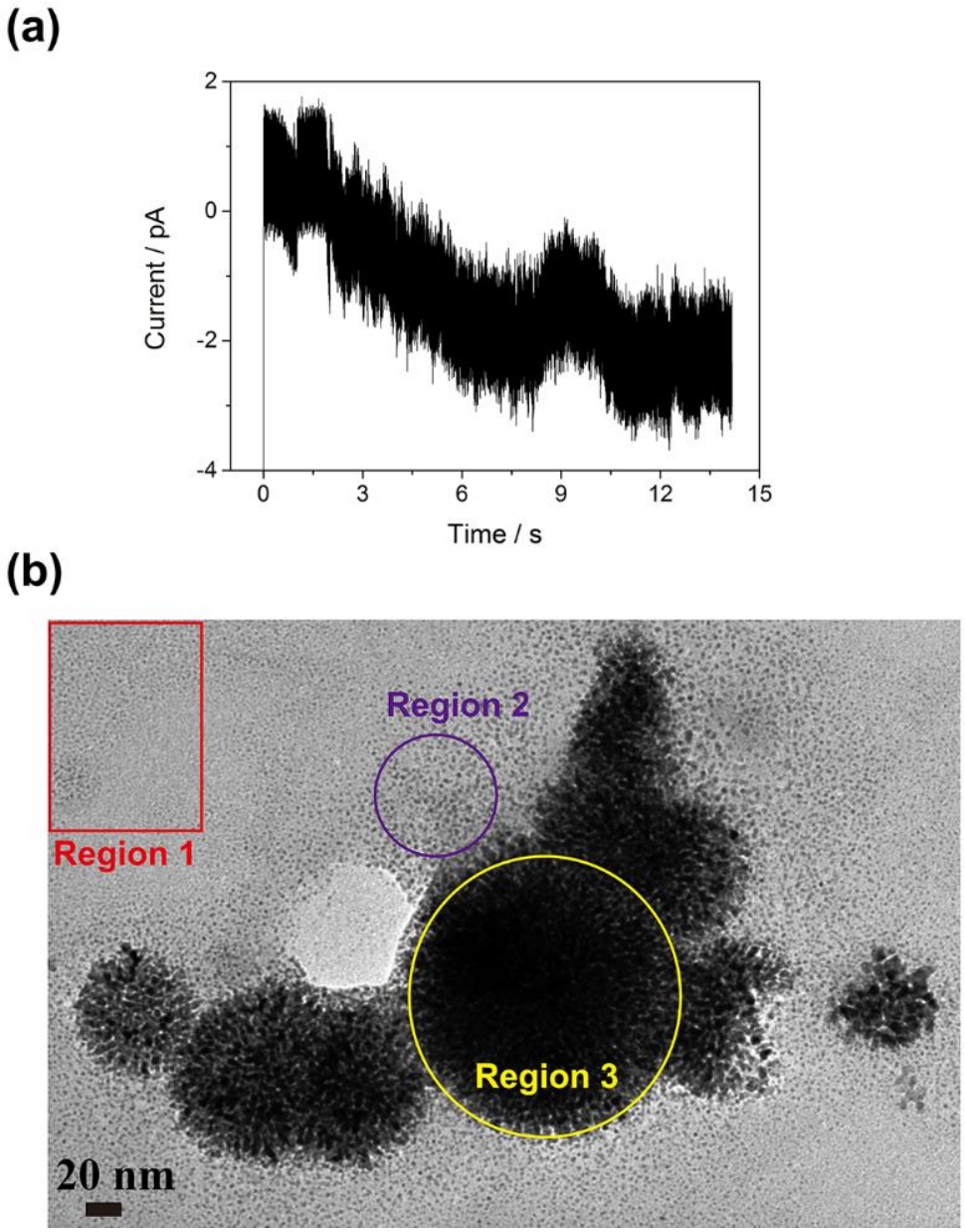

Figure 5. (a) Chronoamperometry data on the TEM grid for Pd electrodeposition at 0.05 V for 14 s. The electrolyte was 1 mM K_2PdCl_4 in 0.1 M $HClO_4$. (b) Image of electrodeposited Pd after 14 s deposition at 0.05 V.

Images of the full region of the experiment and higher magnification images are given in Figure S3, Supporting Information. Among these, the image of the meniscus residue (Figure S3(a)) and particles confirms that meniscus contact occurs over an area similar to the micropipet size (2 μm diameter). Additionally, Figure S4 in Supporting Information shows snapshot optical images taken during the experiment (from below the TEM grid) of a 2 μm diameter micropipet just before meniscus contact with the TEM grid and the electrodeposited Pd after the chronoamperometry experiments.

NPs can be observed in the TEM image shown in Figure 5(b): with an average diameter of 1.0 ± 0.1 nm in region 1 (shown in further detail Figure S3(b), Supporting Information) and an overall diameter of 2.2 ± 0.4 nm in region 2 (shown in further detail Figure S3(c), Supporting Information). The concentration of NPs is of the order of 10^{13} cm^{-2} (7 x 10^{12} cm^{-2} in region 1 and 1.2 x 10^{13} cm^{-2} in region 2). It should further be noted that the smallest NPs were located at a distance of over 100 nm from aggregated large structures, *e.g.* in region 3, which had a characteristic length scale of over 40 nm, and appear to be aggregates of NPs. Indeed, inspection of Figure 5(b) shows a general gradient in the degree of NP aggregation with distance away from the extensive aggregates (region 3).

The TEM images acquired in this study suggest that an aggregative mechanism operates in the electrochemical nucleation and growth of metal NPs,[13,27,28] wherein NPs form and aggregate into larger nanostructures. Assuming that all nanostructures are generated from NPs, which is reasonable based on the TEM images, and that all NPs have spherical shapes, N_0 can also be estimated from the total charge of the reduction current–time curves according to equation (1):

$$N_0 = \frac{3MQ_R}{4\pi^2 r^3 R^2 n\rho F} \quad (1)$$

where M is the molar mass of Pd (106.42 g mol^{-1}), Q_R is the charge passed in the reduction transient (18.3 pC for the transient in Figure 5(a)), r and R are the radii of a single nuclei (0.8 nm, the average value of NPs) and a micropipet (1.0 μm), n is the number of electrons in the electrodeposition process (2), ρ is the density of Pd (12.0 g cm^{-3}),[40] and F is Faraday constant. The value of N_0 is *ca*. 1.0 × 10^{13} particles cm^{-2}, which is of the order found by microscopy.

Evidently, we can view Pd NPs as building blocks for larger nanostructures on the TEM grid. TEM analysis of NPs on the HOPG substrate would be non-trivial, and AFM does not have the resolution to detect NPs of the size seen in TEM, especially when aggregated and closely located. However, the DPSC data provide powerful insight into the number and size of NPs formed. We thus ran DPSC experiments on HOPG at a deposition potential of 0.05 V for different times (Figure 6), and analyzed these data together with the potential-dependent data in Figure 4. The forward step charge (deposition) informs on the amount (volume) of Pd clusters deposited and the reverse step charge (surface oxidation) indicates the surface area. The data together thus enable analysis of the characteristic NP size and their number (Table 1).

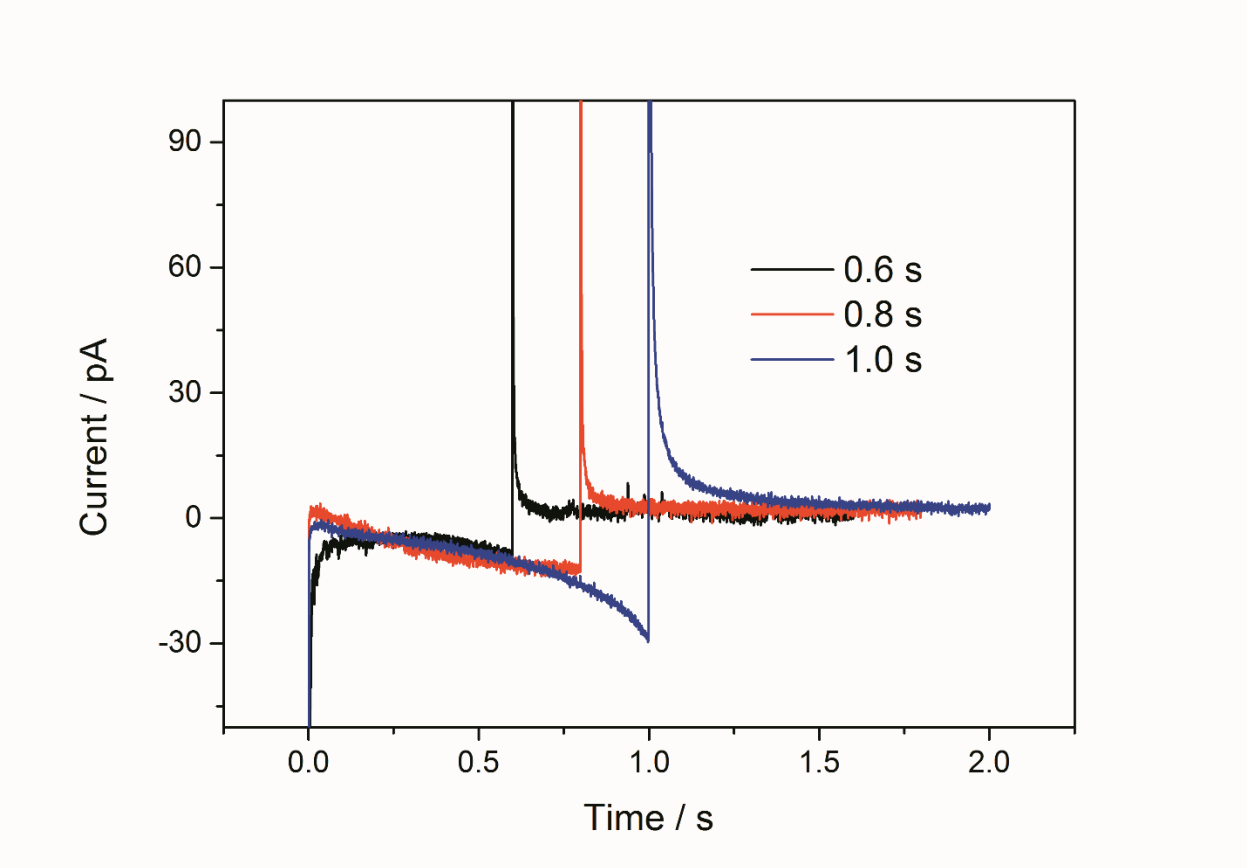

Figure 6. Chronoamperometry data obtained on HOPG for Pd electrodeposition at 0.05 V for various time periods, followed by a step to 1.0 V to promote Pd oxidation for a further 1 s. The electrolyte was 1 mM K_2PdCl_4 in 0.1 M $HClO_4$.

Table 1. Charges for the reduction and oxidation of Pd on HOPG from DPSC experiments (Figures 4 and 6), together with NP size (radius, r) and calculated NP number density

Conditions		Reduction charge (pC)	Oxidation charge (pC)	r (nm)	N_0 (particles cm^{-2})
Potential (V)	Time (s)				
0.05	0.6	3.67	2.15	1.0	1.3×10^{12}
0.05	0.8	5.95	3.16	1.1	1.6×10^{12}
0.05	1.0	10.2	7.20	0.8	6.5×10^{12}
0.035	1.0	25.0	8.51	1.7	1.8×10^{12}
0.025	1.0	45.2	15.5	1.7	3.3×10^{12}

The oxidation charge (Q_O) reflects the electrochemical surface area of the electrodeposited Pd. Thus, the NP number density can also be estimated using the conversion factor (C_f; 424 μC cm^{-2} from Pd to Pd oxide),[41,42] an approach used to determine the area of other Pd nanostructures,[43] and $4\pi r^2$ for the surface area of a spherical NP according to equation (2):

$$Q_O = N_0 \pi R^2 C_f \times 4\pi r^2 \quad (2)$$

The ratio of Q_R to Q_O (equation (3)) obtained from equations (1) and (2), yields the value of r, while substitution of r into equation (1) or (2) yields N_0.

$$\frac{Q_R}{Q_O} = \frac{n\rho F}{MC_f} \times \frac{1}{3} r \quad (3)$$

Given the simplicity of this analysis, radii of NPs on HOPG and N_0 values are evidently in reasonable agreement with the TEM data. Because of aggregation, the electrochemical analysis

will tend to result in a higher value of r, and consequently smaller value of N_0 and this effect becomes generally more significant at higher driving potentials where more material is electrodeposited. Overall, however, the data are broadly consistent with TEM.

From these results, a nucleation and aggregative growth model[13,27,28] appears to operate (Figure 7). The first step is the nucleation and dissolution of discrete NPs, which we consider as a reversible process involving rapid birth (nucleation) and death (dissolution) of NPs unless they attain a critical size (and aggregate) to survive. The standard potential of NPs, E_P^0, shifts cathodically with respect to the bulk value, E_{bulk}^0, with decreasing particle radius:[44]

$$E_P^0 = E_{bulk}^0 - \frac{2\gamma V_M}{zFr} \quad (4)$$

where γ is the surface free energy, V_M is the molar volume, z is the lowest valence state and F is Faraday constant.

It is important to note that NPs, clusters (and adatoms) are not fixed on a substrate, but have considerable mobility especially on HOPG.[26,45] Furthermore, surface diffusion on a substrate can occur thermally[46] and due to electrochemically[47,48] induced migration. This process is thus reasonably consistent with the TEM data and electrochemical measurements.

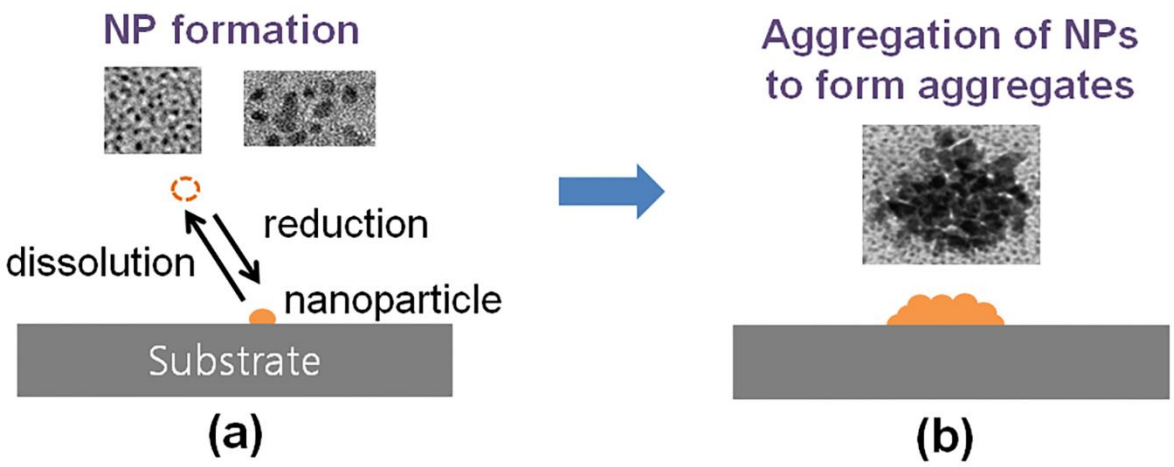

Figure 7. Schematic illustration showing the proposed electrochemical nucleation and growth processes: (a) formation/dissolution of metal NPs and (b) aggregation of NPs to form extensive aggregates.

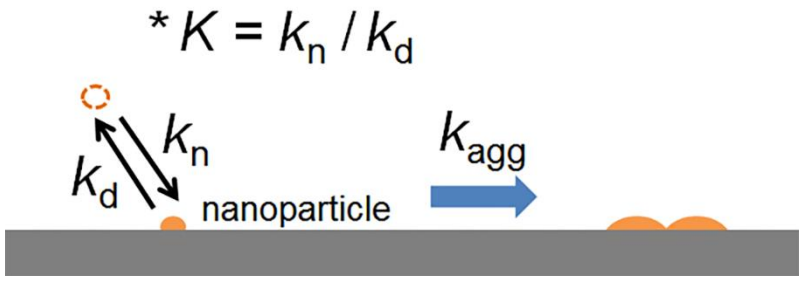

Figure 8. Schematic of nucleation and aggregation processes of metal NPs. k_{n} is a nucleation rate constant, k_{d} is a dissolution rate constant, K is an equilibrium constant and k_{agg} is an aggregation rate constant.

The chronoamperometry data are potentially rich in kinetic information, and having revealed the key entities involved in electrodeposition we propose the main steps shown in Figure 8. The nucleation and dissolution of NPs is potential-dependent and, for simplicity, we adopt a Butler-Volmer formalism, such that the creation and dissolution of clusters are given by k_{n} and k_{d}, defined by equations (5) and (6):

$$k_{\mathrm{n}} = k_0 \exp[-\alpha f(E - E^0)] \quad (5)$$

$$k_{\mathrm{d}} = k_0 \exp[(1-\alpha) f(E - E^0)] \quad (6)$$

where k_0 is a standard rate constant, α is a transfer coefficient and f is nF/RT. This is reasonable given the evident rapidity and extensive nature of NP formation. In any case, in the approach developed below these processes are mainly at a potential-dependent equilibrium, where the kinetic form drops out. On this basis, the observed reduction current is essentially a measure of the number of stable NPs that survive. This is predominantly driven by aggregation, which, in turn, depends on the number of NPs that are aggregated, N_{agg}(an indicator of the aggregate size). At the simplest level, if we assume that aggregation scales in a first-order manner with the number of isolated NPs, N, and those in aggregates, N_{agg}, then:

$$i = nek_{\mathrm{agg}} N N_{\mathrm{agg}} \quad (7)$$

where n is the number of electrons transferred per ion reduction process, and e is a charge of an electron. In the early stages that we consider herein, aggregation is initially a minor route to the overall loss of isolated NPs, and the value of N can be obtained from:

$$\frac{dN}{dt} = k_{\mathrm{n}} - k_{\mathrm{d}}N \quad (8)$$

$$\therefore N = \frac{k_{\mathrm{n}}(1 - e^{-k_d t})}{k_{\mathrm{d}}} = K(1 - e^{-k_d t}) \quad (9)$$

and so

$$i = nek_{\mathrm{agg}}K(1 - e^{-k_d t})N_{\mathrm{agg}} \quad (10)$$

On the basis that NPs mainly end up in aggregates to survive, the value of N_{agg} can be estimated reasonably well from the ratio of $Q_{\mathrm{R}}/Q_{\mathrm{particle}}$, where Q_{particle} is the charge to form a primary NP of 0.8 nm radius, the average size seen in TEM (see above). Further, noting that $e^{-k_d t} \to 0$ for the potentials and times of interest herein, the relationship between i and $Q_{\mathrm{R}}/Q_{\mathrm{particle}}$ is obtained that used to analyze chronoamperometric data:

$$i \approx nek_{\mathrm{agg}}K\,(Q_{\mathrm{R}}/Q_{\mathrm{particle}}) \quad (11)$$

$$i \approx nek_{\mathrm{agg}}\exp[-f(E - E^0)](Q_{\mathrm{R}}/Q_{\mathrm{particle}}) \quad (12)$$

The short-time data from Figure 4 (current values without a significant mass transport component) fit reasonably well to equation 12 at all 3 potentials, the relationship between i and $(Q_{\mathrm{R}}/Q_{\mathrm{particle}})$ is linear and the slope is strongly potential-dependent (Figure 9). Considering that the standard equilibrium potential of $\mathrm{Pd(s) + 4Cl^-} \rightarrow \mathrm{PdCl_4^{2-}(aq) + 2e^-}$ is 0.60 V[49] *versus* NHE and the open circuit potential of the Ag/AgCl QRCE used herein was measured as 0.08 V with respect to Ag/AgCl/KCl (saturated, 0.197 V *versus* NHE). Thus, the experiments herein are around the value (just cathodic of) the standard potential of a 0.8 nm radius NP, estimated to be 0.36 V *versus* NHE (*ca*. 0.08 V *versus* Ag/AgCl QRCE) using 2.05 J $\mathrm{m^{-2}}$ for the surface free energy[50] and 8.85×10^{-6} $\mathrm{m^3\ mol^{-1}}$ for the molar volume of Pd in equation (4). With this value of

the effective standard potential, the following aggregation rate coefficients at the three different potentials are obtained:

$$k_{\mathrm{agg}}(0.05\ \mathrm{V}) = (7.89 \pm 0.01) \times 10^4\ \mathrm{s}^{-1}$$

$$k_{\mathrm{agg}}(0.035\ \mathrm{V}) = (9.57 \pm 0.03) \times 10^4\ \mathrm{s}^{-1}$$

$$k_{\mathrm{agg}}(0.025\ \mathrm{V}) = (8.11 \pm 0.02) \times 10^4\ \mathrm{s}^{-1}$$

Consequently, the aggregation constants are uniform over a relatively small range of potential values (0.05 V to 0.025 V) close to the nucleation potential.

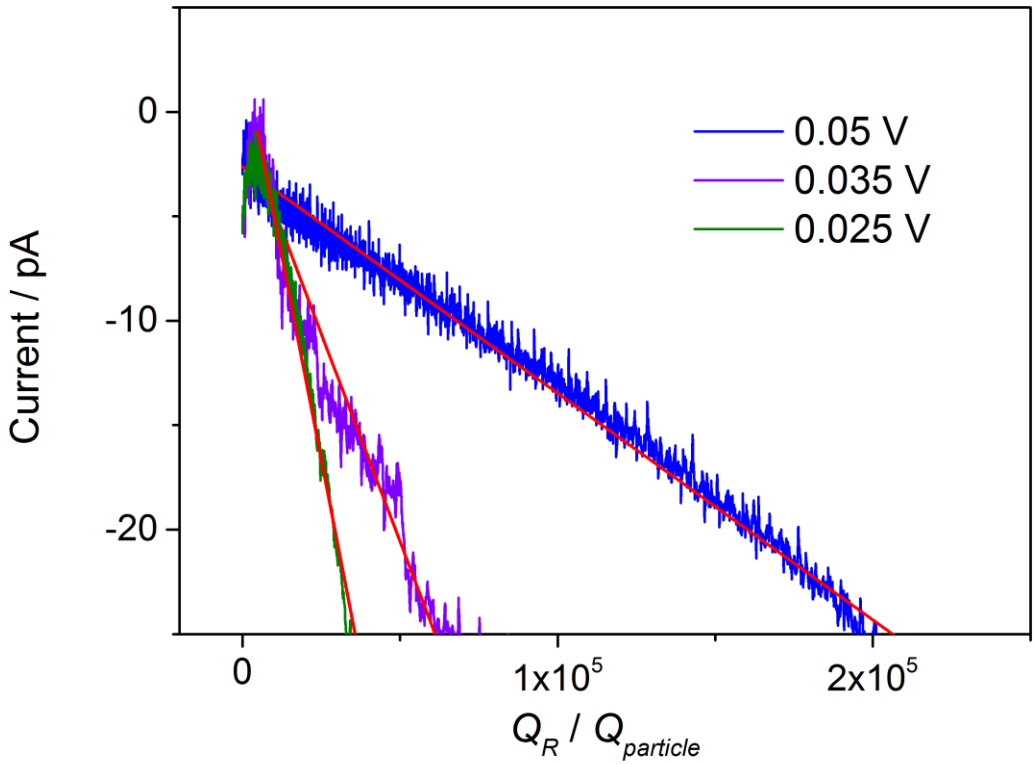

Figure 9. Plots of the reduction current versus $Q_{\mathrm{R}}/Q_{\mathrm{particle}}$ at three different potentials (data from Fig. 4), according to equation (12).

CONCLUSIONS

The electrodeposition of Pd on carbon electrodes has been investigated using a microscale meniscus cell on both HOPG and a TEM grid as the substrate. The microscale meniscus cell has several attributes for these studies. First, it allows electrochemical measurements at a wide variety of substrates, including non-conventional electrodes such as a TEM grid. The electrochemical surface area is defined by the size and position of the micropipet, and the microscale dimensions lead to well-defined mass transport characteristics.

Two types of Pd nanostructures were observed in the electrodeposition processes: NPs with a diameter in the range of 1.0 − 2.2 nm and large aggregates of these elementary NPs, which essentially serve as building blocks. An unusually high density of NPs (10^{13} cm^{-2}) was found in the acquired TEM images. These results demonstrate that the classical nucleation and growth model, which is based on the direct reduction of metal ions on existing nuclei, is not appropriate for the observed nucleation and growth processes.

The aggregative growth model we have developed is based on the assumption that aggregation of elementary NPs is critical for the formation of stable nanostructured palladium. Thus, the charge passed in a chronoamperometric electrodeposition experiment is largely a measure of NPs that are incorporated in larger nanostructures, with isolated NPs continually formed and dissolved at other parts of the surface, giving a population of such structures that can aggregate. We have shown how DPSC, where a forward potential step drives the electrodeposition of Pd (rate measured with the corresponding current-time profile) and a reverse oxidation step converts the Pd surface to oxide, can be analyzed to obtain the number of particles formed, their size, as well as elementary kinetics such as the NP aggregation coefficient.

The simple aggregative growth model described, together with the microscopy studies, provides key insights into the mechanism of Pd electrodeposition. In turn, this model could be extremely useful for the rational electrochemical fabrication of controlled number of NPs on a surface by tuning the deposition time and potential, which would be extremely advantageous for applications in catalysts and sensors. The palladium clusters evidently made in our study are clearly some of the smallest ever reported and could be very interesting as electrocatalysts, in particular.

Supporting Information. Chronoamperometry data without Pd precursor on HOPG, CV data on a TEM grid, and TEM images of electrodeposited Pd. This material is available free of charge via the Internet at http://pubs.acs.org.

ACKNOWLEDGMENT

We thank Dr. Alex W. Colburn and Mr. Binoy Paulose Nadappuram for experimental assistance. This work was supported by a European Research Council Advanced Investigator Grant (ERC-2009-AdG 247143 "QUANTIF") and Basic Science Research Program through the National Research Foundation of Korea (2012R1A6A3A03039226) for Y.-R. Kim.

REFERENCES

1. Roduner, E. Size Matters: Why Nanomaterials Are Different. *Chem. Soc. Rev.* **2006**, *35*, 583-592.

2. Wilcoxon, J. P.; Abrams, B. L. Synthesis, Structure and Properties of Metal Nanoclusters. *Chem. Soc. Rev.* **2006**, *35*, 1162-1194.

3. Burda, C.; Chen, X.; Narayanan, R.; El-Sayed, M. A. Chemistry and Properties of Nanocrystals of Different Shapes. *Chem. Rev*. **2005**, *105*, 1025-1102.

4. Kleijn, S. E. F.; Lai, S. C. S.; Koper, M. T. M.; Unwin, P. R. Electrochemistry of Nanoparticles. *Angew. Chem. Int. Ed.* **2014**, *53*, 3558-3586.

5. Manfrinato, V. R.; Zhang, L.; Su, D.; Duan, H.; Hobbs, R. G.; Stach, E. A.; Berggren, K. K. Resolution Limits of Electron-Beam Lithography toward the Atomic Scale. *Nano Lett.* **2013**, *13*, 1555-1558.

6. Gupta, M. K.; Kulkarni, D. D.; Geryak, R.; Naik, S.; Tsukruk, V. V. A Robust and Facile Approach to Assembling Mobile and Highly-Open Unfrustrated Triangular Lattices from Ferromagnetic Nanorods. *Nano Lett.* **2013**, *13*, 36-42.

7. Chen, H.-W.; Liang, C.-P.; Huang, H.-S.; Chen, J.-G.; Vittal, R.; Lin, C.-Y.; Wu, K. C.-W.; Ho, K-.C. Electrophoretic Deposition of Mesoporous TiO_2 Nanoparticles Consisting of Primary Anatase Nanocrystallites on a Plastic Substrate for Flexible Dye-Sensitized Solar Cells. *Chem. Commun*. **2011**, *47*, 8346-8348.

8. Day, T. M.; Unwin, P. R.; Macpherson J. V. Factors Controlling the Electrodeposition of Metal Nanoparticles on Pristine Single Walled Carbon Nanotubes. *Nano Lett.* **2007**, *7*, 51-57.

9. Xiang, C.; Kung, S.-C.; Taggart, D. K.; Yang, F.; Thompson, M. A.; Güell, A. G.; Yang, Y.; Penner, R. M. Lithographically Patterned Nanowire Electrodeposition: A Method for Patterning Electrically Continuous Metal Nanowires on Dielectrics. *ACS Nano* **2008**, *2*, 1939-1949.

10. Hu, J.; Yu, M.-F. Meniscus-Confined Three-Dimensional Electrodeposition for Direct Writing of Wire Bonds. *Science* **2010**, *329*, 313-316.

11. González-González, I.; Fachini, E. R.; Scibioh, M. A.; Tryk, D. A.; Tague, M.; Abruña, H. D.; Cabrera, C. R. Facet-Selective Platinum Electrodeposition at Free-standing Polycrystalline Boron-Doped Diamond Films. *Langmuir* **2009**, *25*, 10329-10336.

12. Tian, N.; Zhou, Z.-Y.; Sun, S.-G.; Ding, Y.; Wang, Z. L. Synthesis of Tetrahexahedral

Platinum Nanocrystals with High-Index Facets and High Electro-Oxidation Activity. *Science* **2007**, *316*, 732-735.

13. Ustarroz, J.; Ke, X.; Hubin, A.; Bals, S.; Terryn, H. New Insights into the Early Stages of Nanoparticle Electrodeposition. *J. Phys. Chem. C* **2012**, *116*, 2322-2329.

14. *Electrochemical Dictionary*, 2nd, Revised and Extended Edition; Bard, A. J., Inzelt, G., Scholz, F., Eds.; Springer, 2012.

15. Milchev, A. *Electrocrystallization, Fundamentals of Nucleation and Growth*; Kluwer Academic Publishers, 2002.

16. *Electrocrystallization in Nanotechnology*; Staikov, G., Eds.; Wiley-VCH, 2007.

17. Williamson, M. J.; Tromp, R. M.; Vereecken, P. M.; Hull, R.; Ross, F. M. Dynamic Microscopy of Nanoscale Cluster Growth at the Solid–Liquid Interface. *Nat. Mater.* **2003**, *2*, 532-536.

18. Radisic, A.; Vereecken, P. M.; Hannon, J. B.; Searson, P. C.; Ross, F. M. Quantifying Electrochemical Nucleation and Growth of Nanoscale Clusters Using Real-Time Kinetic Data. *Nano Lett.* **2006**, *6*, 238-242.

19. McCreery, R. L. Advanced Carbon Electrode Materials for Molecular Electrochemistry. *Chem. Rev.* **2008**, *108*, 2646-2687.

20. Zheng, H.; Smith, R. K.; Jun, Y.-W.; Kisielowski, C.; Dahmen, U.; Alivisatos, A. P. Observation of Single Colloidal Platinum Nanocrystal Growth Trajectories. *Science* **2009**, *324*, 1309-1312.

21. Evans, J. E.; Jungjohann, K. L.; Browning, N. D.; Arslan, I. Controlled Growth of Nanoparticles from Solution with In Situ Liquid Transmission Electron Microscopy. *Nano Lett.* **2011**, *11*, 2809-2813.

22. Liao, H.-G.; Cui, L.; Whitelam, S.; Zheng, H. Real-Time Imaging of Pt_3Fe Nanorod Growth in Solution. *Science* **2012**, *336*, 1011-1014.

23. Zhang, B.; Ye, D.; Li, J.; Zhu, X.; Liao, Q. Electrodeposition of Pd Catalyst Layer on Graphite Rod Electrodes for Direct Formic Acid Oxidation. *J. Power Sources* **2012**, *214*, 277-284.

24. Kim, B.-K.; Seo, D.; Lee, J. Y.; Song, H.; Kwak, J. Electrochemical Deposition of Pd Nanoparticles on Indium-Tin Oxide Electrodes and Their Catalytic Properties for Formic Acid Oxidation. *Electrochem. Commun*. **2010**, *12*, 1442-1445.

25. Williams, C. G.; Edwards, M. A.; Colley, A. L.; Macpherson, J. V.; Unwin, P. R. Scanning Micropipet Contact Method for High-Resolution Imaging of Electrode Surface Redox Activity. *Anal*. *Chem*. **2009**, *81*, 2486-2495.

26. Lai, S. C. S.; Lazenby, R. A.; Kirkman, P. M.; Unwin, P. R. Nucleation, Aggregative Growth and Detachment of Metal Nanoparticles during Electrodeposition at Electrode Surfaces. *Chem*. *Sci*. **2015**, 6, 1126-1138.

27. Ustarroz, J.; Gupta, U.; Hubin, A.; Bals, S.; Terryn, H. Electrodeposition of Ag Nanoparticles onto Carbon Coated TEM Grids: A Direct Approach to Study Early Stages of Nucleation. *Electrochem. Commun*. **2010**, *12*, 1706-1709.

28. Ustarroz, J.; Hammons, J. A.; Altantzis, T.; Hubin, A.; Bals, S.; Terryn, H. A Generalized Electrochemical Aggregative Growth Mechanism. *J. Am. Chem. Soc*. **2013**, *135*, 11550-11561.

29. Patel, A. N.; Collignon, M. G.; O'Connell, M. A.; Hung, W. O. Y.; McKelvey, K.; Macpherson, J. V.; Unwin, P. R. A New View of Electrochemistry at Highly Oriented Pyrolytic Graphite. *J. Am. Chem. Soc.* **2012**, *134*, 20117-20130.

30. Liu, H.; Favier, F.; Ng, K.; Zach, M. P.; Penner, R. M. Size-Selective Electrodeposition of

Meso-Scale Metal Particles: A General Method. *Electrochim. Acta* **2001**, *47*, 671-677.

31. Gimeno, Y.; Hernández Creus, A.; Carro, P.; González, S.; Salvarezza, R. C.; Arvia A. J. Electrochemical Formation of Palladium Islands on HOPG: Kinetics, Morphology, and Growth Mechanisms. *J. Phys. Chem. B* **2002**, *106*, 4232-4244.

32. Bayati, M.; Abad, J. M.; Nichols, R. J.; Schiffrin, D. J. Substrate Structural Effects on the Synthesis and Electrochemical Properties of Platinum Nanoparticles on Highly Oriented Pyrolytic Graphite. *J. Phys. Chem. C* **2010**, *114*, 18439-18448.

33. Lai, S. C. S.; Patel, A. N.; McKelvey, K.; Unwin, P. R. Definitive Evidence for Fast Electron Transfer at Pristine Basal Plane Graphite from High-Resolution Electrochemical Imaging. *Angew. Chem. Int. Ed.* **2012**, *51*, 5405-5408.

34. Güell, A. G.; Meadows, K. E.; Dudin, P. V.; Ebejer, N.; Macpherson, J. V.; Unwin, P. R. Mapping Nanoscale Electrochemistry of Individual Single-Walled Carbon Nanotubes. *Nano Lett*. **2014**, *14*, 220-224.

35. Dudin, P. V.; Snowden, M. E.; Macpherson, J. V.; Unwin, P. R. Electrochemistry at Nanoscale Electrodes: Individual Single-Walled Carbon Nanotubes (SWNTs) and SWNT-Templated Metal Nanowires. *ACS Nano* **2011**, *5*, 10017-10025.

36. Kleijn, S. E. F.; Lai, S. C. S.; Miller, T. S.; Yanson, A. I.; Koper, M. T. M.; Unwin, P. R. Landing and Catalytic Characterization of Individual Nanoparticles on Electrode Surfaces. *J. Am. Chem. Soc*. **2012**, *134*, 18558-18561.

37. Corduneanu, O.; Diculescu, V. C.; Chiorcea-Paquim, A.-M.; Oliveira-Brett, A.-M. Shape-Controlled Palladium Nanowires and Nanoparticles Electrodeposited on Carbon Electrodes. *J. Electroanal. Chem.* **2008**, *624*, 97-108.

38. Burke, L. D. Premonolayer Oxidation and Its Role in Electrocatalysis. *Electrochim. Acta*.

1994, *39*, 1841-1848.

39. Bard, A. J.; Faulkner, L. R. *Electrochemical Methods, Fundamentals and Applications*, 2nd ed.; John Wiley and Sons: New York, 2001.

40. Tasaltin, N.; Öztürk, S.; Kilinc, N.; Yüzer, H.; Öztürk, Z. Z. Fabrication of Vertically Aligned Pd Nanowire Array in AAO Template by Electrodeposition Using Neutral Electrolyte. *Nanoscale Res. Lett.* **2010**, *5*, 1137-1143.

41. Rand, D. A. J.; Woods, R. The Nature of Adsorbed Oxygen on Rhodium, Palladium and Gold Electrodes. *J. Electroanal. Chem*. **1971**, *31*, 29-38.

42. Xiao, L.; Zhuang, L.; Liu, Y.; Lu, J.; Abruña, H. D. Activating Pd by Morphology Tailoring for Oxygen Reduction. *J. Am. Chem. Soc.* **2009**, *131*, 602-608.

43. Tian, N.; Zhou, Z.-Y.; Sun, S.-G. Electrochemical Preparation of Pd Nanorods with High-Index Facets. *Chem. Commun*. **2009**, 1502-1504.

44. Redmond, P. L.; Hallock, A. J.; Brus, L. E. Electrochemical Ostwald Ripening of Colloidal Ag Particles on Conductive Substrates. *Nano Lett.* **2005**, *5*, 131-135.

45. Lewis, L. J.; Jensen, P.; Combe, N.; Barrat, J.-L. Diffusion of Gold nanoclusters on Graphite. *Phys. Rev. B* **2000**, *61*, 16084.

46. Thiel, P. A.; Shen, M.; Liu, D.-J.; Evans, J. W. Coarsening of Two-Dimensional Nanoclusters on Metal Surfaces. *J. Phys. Chem. C* **2009**, *113*, 5047-5067.

47. Dudin, P. V.; Unwin, P. R.; Macpherson, J. V. Electrochemical Nucleation and Growth of Gold Nanoparticles on Single-Walled Carbon Nanotubes: New Mechanistic Insights. *J. Phys. Chem. C* **2010**, *114*, 13241-13248.

48. Hartl, K.; Nesselberger, M.; Mayrhofer, K. J. J.; Kunz, S.; Schweinberger, F. F.; Kwon, G.; Hanzlik, M.; Heiz, U.; Arenz, M. Electrochemically Induced Nanocluster Migration.

Electrochim. Acta **2010**, *56*, 810-816.

49. *Encyclopedia of Electrochemistry, Volume 7a: Inorganic Electrochemistry*; Bard, A. J., Stratmann, M., Eds.; Wiley-VCH: Weinheim, Germany, 2006; p 511.

50. Li, Z.; Gao, F.; Wang, Y.; Calaza, F.; Burkholder, L.; Tysoe, W. T. Formation and Characterization of Au/Pd surface Alloys on Pd(1 1 1). *Surf. Sci.* **2007**, *601*, 1898-1908.

Table of Contents